

A T-matrix scattering formalism for electron-beam spectroscopy

P. Elli Stamatopoulou  ^{1, 2, *} and Carsten Rockstuhl  ^{1, 3, 4, †}

¹ Institute of Nanotechnology, Karlsruhe Institute of Technology, Kaiserstr. 12, DE-76131, Germany

² POLIMA—Center for Polariton-driven Light—Matter Interactions,

University of Southern Denmark, Campusvej 55, DK-5230 Odense M, Denmark

³ Institute of Theoretical Solid State Physics, Karlsruhe Institute of Technology, Kaiserstr. 12, DE-76131, Germany

⁴ Center for Integrated Quantum Science and Technology (IQST),

Karlsruhe Institute of Technology, Wolfgang-Gaede-Str. 1, 76131 Karlsruhe, Germany

(Dated: February 16, 2026)

Advanced computational tools that describe the interaction of electrons with structured nanophotonic materials are crucial for theoretical predictions, specific design tasks, and the interpretation of experimental results. These tools open the door to systematic exploration of free-electron–driven nanophotonic light sources, among others. Here, we report on the implementation of electron-beam spectroscopy in a T-matrix-based scattering formulation. Such a framework is quite versatile in predicting the electromagnetic response of complex photonic materials composed of periodically or aperiodically arranged individual scatterers. By extending this formalism to describe interactions with fast electrons, we provide a fast and accurate numerical tool for simulating cathodoluminescence (CL) and electron energy-loss spectroscopy (EELS) measurements. The desired functionalities are implemented into the existing software suite *treams* for electromagnetic scattering computations, and the extended code *treams_ebeam* is available online at https://github.com/tfp-photonics/treams_ebeam. We demonstrate the implementation details on a carefully selected set of problems, including single scatterers of various shapes and materials, a periodic chain of elliptical nanodisks, and a finite cluster of nanospheres arranged in a two-dimensional (2D) lattice. By uniting fast-electron physics with advanced scattering theory, our framework unlocks new possibilities for designing, understanding, and engineering next-generation nanoscale light–matter interactions.

I. INTRODUCTION

In recent years, electron-beam spectroscopy has proven indispensable for exploring the optical properties of matter. Fast electrons passing by a sample transfer energy to the optical modes sustained therein, which can then be detected in two complementary techniques [1]. In cathodoluminescence (CL) spectroscopy, a tightly focused electron beam is scanned over a specimen in an electron microscope, while the far-field emission released from the sample is collected and analyzed to reveal the radiative decay pathways of its optical excitations [2, 3]. Electron energy-loss spectroscopy (EELS), performed in the transmission configuration of the electron microscope, instead detects the total energy lost by the beam, thus capturing both radiative and dark optical modes [4]. Remarkable progress in theoretical and experimental approaches in both techniques has led to an unprecedented combination of spatial, energy, and—most recently—temporal resolution [5, 6].

Unlike in traditional light-based spectroscopic methods, fast electrons can access the near field of a photonic structure because the electromagnetic fields generated by their motion are evanescent. At the same time, they are spectrally broadband, and can excite different collective phenomena across a wide range of frequencies, from bulk and surface plasmons in metals [7–10] and Mie resonances in dielectric nanocavities [11–13] in the optical spectrum, to THz bulk and surface phonons in polar crystals [14–17] and magnons in magnetic materials [18]. Owing to these characteristics, fast electrons are powerful probes for studying more complex photonic platforms designed for greater optical control, such as nanoantennas, photonic crystals, or metasurfaces, which comprise multiple scatterers, often in periodic arrangements. Such interactions have already been investigated, though not extensively, for the generation of Smith–Purcell [19–21] and Cherenkov radiation [22], or bound (BICs) and quasi-bound states in the continuum (q-BICs) [23].

As photonic platforms grow in complexity, so does the need for robust numerical tools capable of modeling the free electron–matter interaction efficiently. In this regard, several methods have been devised for CL and EELS simulations. These include the boundary element method (BEM) [24, 25], the finite element method (FEM) [23, 26], the finite-difference time-domain (FDTD) method [27, 28], the discrete dipole approximation (DDA) [29], or the discontinuous Galerkin time-domain (DGTD) method [30–33]. While these approaches undeniably have their merits, they rely on solving Maxwell’s equations in discretized space and/or time, rendering them computationally expensive and time-consuming, even prohibitive for systems involving multiple length scales or requiring extensive parameter sweeps. Furthermore, modeling infinitely extended periodic structures remains a challenge for some of these methods. An alternative approach that overcomes these limitations is the T-matrix method [34–36]. In this framework, the fields

scattered by an object are related to the illumination via the T-matrix, which encodes all material and geometrical parameters of the entire structure, while it is otherwise independent of the illumination. The computational benefit comes from the fact that the T-matrix only needs to be retrieved once for a given object, and can be stored and reused for later computations [37, 38]. Moreover, the response to electron beams from complex photonic materials made from many scatterers can conveniently be expressed within an algebraic formulation [39–42]. Early theoretical efforts in electron-beam spectroscopy employed the T-matrix method to study the individual and collective resonances in spherically and cylindrically symmetric nanoparticles and assemblies thereof [43–47].

Here, we present a general framework of CL and EELS simulations based on the T-matrix method, applicable to one or more scatterers of arbitrary shapes and aloof electron beams. The manuscript is structured as follows. We first outline the theory, where we express the field of a fast electron in the appropriate basis so that it can be considered in the T-matrix formalism. We then focus on its interaction with a scatterer, demonstrating the relation connecting the scattered and incident fields via the T-matrix formalism, which we extend to account for multiple periodically or aperiodically arranged scatterers. Based on this formalism, we show the resulting expressions for computing the CL and electron energy-loss (EEL) probabilities. In the following section, we demonstrate the capabilities of our approach through three representative examples: single scatterers of various shapes, a periodic chain of elliptical nanodisks, and a finite cluster of nanospheres arranged in a two-dimensional (2D) lattice. We discuss our numerical implementation of this framework within the Python package *treams*, providing guidance on its use [48]. We close with our concluding remarks.

II. THEORY

This section outlines the theoretical framework underlying our description of the interaction of electrons with structured nanophotonic materials, progressing from the field representation of a fast electron to experimentally accessible observables. We first formulate the electromagnetic field of a relativistic electron in a cylindrical wave basis (CWB), which provides a natural and efficient representation for an electron moving along a straight trajectory. We then describe the interaction of the electron with complex photonic nanostructures composed of isolated scatterers and of ensembles thereof, arranged periodically or aperiodically. Eventually, we show how the same formalism yields unified expressions for CL and EEL probabilities, directly linking theory to measurable radiation and dissipation channels.

A. Electromagnetic field of a fast electron in the cylindrical wave basis

We start by expressing the electromagnetic fields of an electron traveling with constant velocity in the angular-frequency (ω) domain in the CWB, using a cylindrical coordinate system $\mathbf{r} = (\rho, \phi, z)$. The choice of basis is motivated by the fact that the fields of the electron take the form of a transverse magnetic (TM) cylindrical wave, as we demonstrate in what follows. We note here that all relevant fields in the present T-matrix formalism considering aloof electron beams are expressed in vacuum or air with relative permittivity and permeability equal to unity.

The electric field $\mathbf{E}(\mathbf{r}, \omega)$ of an electromagnetic wave can be written in the following general form in the CWB [49]:

$$\mathbf{E}(\mathbf{r}, \omega) = \sum_{m=-\infty}^{+\infty} \int_0^\infty dk_z \left[a_{k_z m} \mathbf{N}_{k_z m}^{(n)}(\mathbf{r}, \omega) + b_{k_z m} \mathbf{M}_{k_z m}^{(n)}(\mathbf{r}, \omega) \right], \quad (1)$$

where $\mathbf{N}_{k_z m}^{(n)}(\mathbf{r}, \omega)$ and $\mathbf{M}_{k_z m}^{(n)}(\mathbf{r}, \omega)$ are vector cylindrical wave functions of kind n , describing vector cylindrical waves of transverse magnetic (TM) and transverse electric (TE) polarization, respectively. They are characterized by wavenumber $k(\omega) = \omega/c$, where $c = 1/\sqrt{\varepsilon_0 \mu_0}$ is the speed of light in vacuum, and ε_0, μ_0 are the vacuum permittivity and permeability, respectively. The vector cylindrical waves are indexed by the z -component of their wavevector k_z and the azimuthal index $m \in \mathbb{Z}$. Furthermore, $a_{k_z m}$ and $b_{k_z m}$ are the corresponding expansion coefficients that express the contribution of a given vector cylindrical wave to the electric field. The basis functions of the vector cylindrical waves in a cylindrical coordinate system characterized by the basis vector $\hat{\rho}$, $\hat{\phi}$, and \hat{z} are given by the following relations:

$$\mathbf{N}_{k_z m}^{(n)}(\mathbf{r}, \omega) = \left(\frac{ik_z}{k} Z_m^{(n)}(k_\rho \rho) \hat{\rho} - \frac{k_z m}{kk_\rho \rho} Z_m^{(n)'}(k_\rho \rho) \hat{\phi} + \frac{k_\rho}{k} Z_m^{(n)}(k_\rho \rho) \hat{z} \right) e^{im\phi + ik_z z}, \quad (2a)$$

$$\mathbf{M}_{k_z m}^{(n)}(\mathbf{r}, \omega) = \left(\frac{im}{k_\rho \rho} Z_m^{(n)}(k_\rho \rho) \hat{\rho} - Z_m^{(n)'}(k_\rho \rho) \hat{\phi} \right) e^{im\phi + ik_z z}, \quad (2b)$$

where $k_\rho(\omega) = \sqrt{(\omega/c)^2 - k_z^2}$ is the wavevector component in the radial direction. For notational simplicity, in Eqs. (2) and in what follows, the explicit dependence of k and k_ρ on ω is omitted. The function $Z_m^{(n)}(x)$ can be the Bessel or Hankel function of the first or second kind, respectively. As usual for T-matrices, we choose $Z_m^{(1)}(x) = J_m(x)$ to describe waves that must be regular in the whole space, and $Z_m^{(3)}(x) = H_m^{(+)}(x)$ for those that must fulfill the radiation condition. Henceforth, we refer to these two types of waves as *regular* and *singular*, respectively.

We now consider an electron carrying the elementary charge e and traveling along the z axis with constant velocity $\mathbf{v} = v\hat{\mathbf{z}}$, such that its trajectory is given by $\mathbf{r}_e = \mathbf{vt}$. At time $t = 0$, the electron lies at the origin of the axes. The electric field for this case can be found in literature [50], and it reads:

$$\mathbf{E}(\mathbf{r}, \omega) = -\frac{e}{2\pi\epsilon_0} \frac{\omega}{v^2\gamma} e^{i\omega z/v} \left[K_1 \left(\frac{\omega\rho}{v\gamma} \right) \hat{\mathbf{p}} - \frac{i}{\gamma} K_0 \left(\frac{\omega\rho}{v\gamma} \right) \hat{\mathbf{z}} \right], \quad (3)$$

where $\gamma = 1/\sqrt{1 - \beta^2}$ is the Lorentz boost, with $\beta = v/c$ being the reduced velocity. Here, $K_m(x)$ denotes the modified Bessel function of order m . To express the field in the basis of Eq. (1), we apply the connection formulas $K_m(x) = \pi i^{m+1} H_m^{(+)}(ix)/2$, and rewrite Eq. (3) as

$$\mathbf{E}(\mathbf{r}, \omega) = \frac{e}{4\epsilon_0} \frac{\omega}{v^2\gamma} e^{i\omega z/v} \left[H_1^{(+)} \left(\frac{i\omega\rho}{v\gamma} \right) \hat{\mathbf{p}} - \frac{1}{\gamma} H_0^{(+)} \left(\frac{i\omega\rho}{v\gamma} \right) \hat{\mathbf{z}} \right]. \quad (4)$$

As a next step, we use the property of Hankel functions $H_1^{(+)}(x) = -H_0^{(+)}'(x)$, and find

$$\mathbf{E}(\mathbf{r}, \omega) = -\frac{e}{4\epsilon_0} \frac{\omega}{v^2\gamma} e^{i\omega z/v} \left[H_0^{(+)}' \left(\frac{i\omega\rho}{v\gamma} \right) \hat{\mathbf{p}} + \frac{1}{\gamma} H_0^{(+)} \left(\frac{i\omega\rho}{v\gamma} \right) \hat{\mathbf{z}} \right]. \quad (5)$$

By introducing $k_z = \omega/v$ and $k_\rho = \sqrt{k^2 - k_z^2} = i\omega/(v\gamma)$, we obtain

$$\mathbf{E}(\mathbf{r}, \omega) = \frac{ie}{4\epsilon_0} \frac{k_z}{c\gamma} e^{ik_z z} \left[\frac{ik_z}{k} H_0^{(+)}' (k_\rho\rho) \hat{\mathbf{p}} + \frac{k_\rho}{k} H_0^{(+)} (k_\rho\rho) \hat{\mathbf{z}} \right]. \quad (6)$$

Compared with Eqs. (1) and (2), Eq. (6) reveals that the field produced by the electron is a purely TM-polarized cylindrical wave of singular type, order $m = 0$ and fixed k_z , whose amplitude is given by $a_{k_z 0} = iek_z/(4\epsilon_0 c\gamma)$. Furthermore, if we express k_z in terms of the wavenumber, we find $k_z = k/\beta > k$ and $k_\rho = ik_z/(\beta\gamma) \in \mathbb{I}$, with \mathbb{I} denoting the set of imaginary numbers. Therefore, the cylindrical wave propagates along the electron trajectory and is evanescent normal to it. Interestingly, the excitation of a nanostructure by a fast electron is one of the few electromagnetic scattering problems that is often best formulated in terms of cylindrical rather than spherical or plane waves. In the following section, we focus on this interaction and discuss in more detail the choice of basis for the expansion of the relevant fields.

B. Interaction of a fast electron with nanostructures

We now consider the interaction of a fast electron with a scatterer of arbitrary shape, as shown in Fig. 1(a). The incident field of the electron excites the optical modes of the object, leading to an additional scattered field. The incident and scattered fields, which constitute the total field, can be expanded as

$$\mathbf{E}_{\text{inc}}(\mathbf{r}, \omega) = \sum_{\nu} \sum_{\lambda=0,1} a_{\nu\lambda} \mathbf{F}_{\nu\lambda}^{(1)}(\mathbf{r}, \omega), \quad (7a)$$

$$\mathbf{E}_{\text{sca}}(\mathbf{r}, \omega) = \sum_{\nu} \sum_{\lambda=0,1} p_{\nu\lambda} \mathbf{F}_{\nu\lambda}^{(3)}(\mathbf{r}, \omega), \quad (7b)$$

where ν is a generalized index condensing all other indices used to expand the field, λ is a polarization index, and $\mathbf{F}_{\nu\lambda}^{(n)}(\mathbf{r}, \omega)$ are the basis vector functions. To connect this notation with the formulas in Section II A, in the CWB we have $\nu = k_z, m$, while $\mathbf{F}_{\nu 0}^{(n)}(\mathbf{r}, \omega) = \mathbf{N}_{k_z m}^{(n)}(\mathbf{r}, \omega)$ for TM polarization ($\lambda = 0$), and $\mathbf{F}_{\nu 1}^{(n)}(\mathbf{r}, \omega) = \mathbf{M}_{k_z m}^{(n)}(\mathbf{r}, \omega)$ for TE polarization ($\lambda = 1$). In the SWB, $\nu = \ell, m$, while $\mathbf{F}_{\nu 0}^{(n)}(\mathbf{r}, \omega) = \mathbf{N}_{\ell m}^{(n)}(\mathbf{r}, \omega)$ for TM polarization, and $\mathbf{F}_{\nu 1}^{(n)}(\mathbf{r}, \omega) = \mathbf{M}_{\ell m}^{(n)}(\mathbf{r}, \omega)$ for TE polarization, with ℓ, m denoting the angular momentum indices with $-\ell \leq m \leq \ell$.

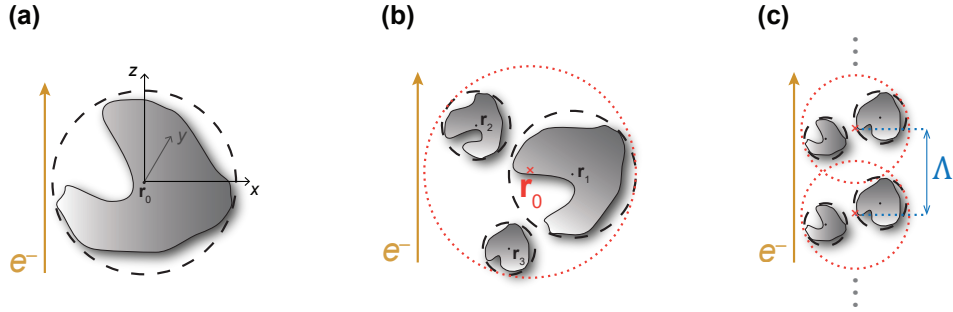


FIG. 1. Examples of scatterer configurations excited by an electron beam, along with the validity domains of the relevant field expansions in the SWB. (a) For a scatterer of arbitrary shape the validity domain is outside the circumscribing sphere enclosing the scatterer, outlined with the dashed black circle. (b) Cluster with three scatterers. In a local description, the fields are expanded at the position \mathbf{r}_i of the i th scatterer, and are valid outside the corresponding circumscribing sphere (black dashed circle). The red dotted circle indicates the validity domain of the global description, which lies outside the circumscribing sphere enclosing all scatterers. (c) Infinite one-dimensional (1D) array with pitch $\Lambda = \Lambda \hat{\mathbf{z}}$ with a complex unit cell, composed of two scatterers. The red dotted circles mark the domain of validity for a global T-matrix, describing the scatterers of the unit cell as a combined object. This description might be invalid due to overlapping circumscribing spheres, in which case only the local description (black dashed circles) can be employed.

The basis vectors in the SWB take the general form [49]

$$\mathbf{N}_{\ell m}^{(n)}(\mathbf{r}, \omega) = N_{\ell m}[\mathrm{i}\pi_{\ell m}(\theta)\hat{\Theta} - \tau_{\ell m}(\theta)\hat{\Phi}] = \mathbf{X}_{\ell m}(\theta, \phi)z_{\ell}^{(n)}(kr), \quad (8a)$$

$$\mathbf{M}_{\ell m}^{(n)}(\mathbf{r}, \omega) = \left[\mathrm{i}\sqrt{\ell(\ell+1)}Y_{\ell m}(\theta, \phi)\frac{z_{\ell}^{(n)}(kr)}{kr}\hat{\mathbf{r}} + \left(z_{\ell}^{(n)'}(kr) + \frac{z_{\ell}^{(n)}(kr)}{kr}\hat{\mathbf{r}} \times \mathbf{X}_{\ell m}(\theta, \phi) \right) \right], \quad (8b)$$

where

$$N_{\ell m} = \mathrm{i}\sqrt{\frac{(2\ell+1)}{4\pi\ell(\ell+1)}\frac{(\ell-m)!}{(\ell+m)!}}, \quad \pi_{\ell m}(\theta) = \frac{mP_{\ell}^m(\cos\theta)}{\sin\theta}, \quad \tau_{\ell m}(\theta) = \frac{\partial P_{\ell}^m(\cos\theta)}{\partial\theta}. \quad (9)$$

In Eq. (8), $Y_{\ell m}(\theta, \phi)$ are the scalar spherical harmonics, $\mathbf{X}_{\ell m}(\theta, \phi)$ are the vector spherical harmonics, and the angular functions $\pi_{\ell m}(\theta)$ and $\tau_{\ell m}(\theta)$ are derived from the Legendre polynomials $P_{\ell}^m(\cos\theta)$. The radial dependence of the basis vectors is given by spherical Bessel-type functions, where $z_{\ell}^{(1)}(x) = j_{\ell}(x)$ are spherical Bessel functions of the first kind (regular modes) and $z_{\ell}^{(3)}(x) = h_{\ell}^{(+)}(x)$ spherical Hankel functions of the first kind (singular modes). For all formulas and basis vectors presented here, we use the conventions found in Ref. 48. We emphasize that the spherical-wave expansion of the fields given in Eq. (7) is valid only outside the circumscribing sphere enclosing the scatterer, as indicated in Fig. 1(a) with the dashed black circle. Consequently, an electron beam that intersects the invalid domain cannot be described by Eq. (7a).

In Section II A, we expressed the field of the electron in singular waves in Eq. (6), whereas in Eq. (7a) it is expanded in regular waves. To convert a singular cylindrical wave at point \mathbf{r} to a regular one at \mathbf{r}' , we use the expression [51]

$$\mathbf{F}_{k_z m}^{(3)}(\mathbf{r}, \omega) = \sum_{m'=-\infty}^{\infty} H_{m-m'}^{(+)}\left(\sqrt{k^2 - k_z^2}\rho_{r-r'}\right) e^{i(m-m')\phi_{r-r'} + ik_z(z-z')}\mathbf{F}_{k_z m'}^{(1)}(\mathbf{r}', \omega). \quad (10)$$

Furthermore, we can expand the incident field of a fast electron in the SWB using the relations connecting regular cylindrical and regular spherical waves, given by [52]

$$\begin{pmatrix} \mathbf{M}_{k_z m}^{(1)}(\mathbf{r}, \omega) \\ \mathbf{N}_{k_z m}^{(1)}(\mathbf{r}, \omega) \end{pmatrix} = \sum_{\ell=m}^{\infty} 4\pi i^{\ell-m} N_{\ell m} e^{im\phi_k} \begin{pmatrix} \tau_{\ell m}(\theta_k) & \pi_{\ell m}(\theta_k) \\ \pi_{\ell m}(\theta_k) & \tau_{\ell m}(\theta_k) \end{pmatrix} \begin{pmatrix} \mathbf{M}_{\ell m}^{(1)}(\mathbf{r}, \omega) \\ \mathbf{N}_{\ell m}^{(1)}(\mathbf{r}, \omega) \end{pmatrix}, \quad (11)$$

where θ_k and ϕ_k are the angles of the wavevector $\mathbf{k} = (k, \theta_k, \phi_k)$ in spherical coordinates.

Returning to Eq. (7), the expansion coefficients of the scattered and incident waves in a linear response theory are related via a T-matrix as

$$\mathbf{p} = \mathbf{T} \mathbf{a}. \quad (12)$$

The T-matrix of an object encodes all material and geometrical properties that determine its optical response to an illumination. To perform the matrix multiplication of Eq. (12), both the T-matrix and the illumination must be represented in the same basis. Whether the object is best described by a spherical or a cylindrical T-matrix depends on its symmetry. Scatterers of finite dimensions and arbitrary shapes are most commonly described by spherical T-matrices, whereas cylindrical T-matrices are naturally suited for scatterers with translational symmetry along one axis, such as cylinders or one-dimensional (1D) periodic chains of scatterers. Analytic formulas exist for spheres in the SWB and infinitely long cylinders in the CWB [49]. For other geometries, the T-matrix can be computed numerically. Reference 37 offers an overview of computations of spherical T-matrices using various numerical Maxwell solvers. Concerning the illumination, generally the CWB is well-suited for incident fields with fixed k_z , as is the case of fast electrons, and can be readily expanded to the basis of the T-matrix characterizing the scatterer using Eqs. (10) and (11).

The T-matrix method provides an elegant framework for multiple scattering in ensembles of nanostructures. Consider N scatterers at positions \mathbf{r}_i with $i = 1, 2, \dots, N$, each one described by a T-matrix \mathbf{T}_i . To describe the scattered field at scatterer i , one has to include the scattered field of all other scatterers as an incident field in addition to the incident field \mathbf{a} of the fast electron, as

$$\mathbf{p}_i = \mathbf{T}_i \left[\mathbf{a}_i + \sum_{j \neq i}^N \mathbf{C}^{(3)}(\mathbf{r}_i - \mathbf{r}_j) \mathbf{p}_j \right], \quad (13)$$

where $\mathbf{C}^{(3)}(\mathbf{r}_i - \mathbf{r}_j) = \mathbf{C}_{i,j}^{(3)}$ contains the translation coefficients along $\mathbf{r}_i - \mathbf{r}_j$. We refer the reader to Ref. 48 for the formulas of the translation coefficients. Figure 1(b) shows an example of a cluster with three scatterers. In a local description, the field expansions \mathbf{a}_i and \mathbf{p}_i are expressed in a SWB centered at the position of the i th scatterer, and are valid outside the corresponding circumscribing sphere (black dashed circle), which must not overlap. By combining all field expansions in a single vector $\mathbf{a}_{\text{local}}$ and $\mathbf{p}_{\text{local}}$, Eq. (13) can be recast in a form similar to Eq. (12), as

$$\mathbf{p}_{\text{local}} = \mathbf{T}_{\text{local}} \mathbf{a}_{\text{local}}, \quad (14)$$

where

$$\mathbf{T}_{\text{local}} = [\mathbb{I} - \mathbf{T}_{\text{diag}} \mathbf{C}^{(3)}]^{-1} \mathbf{T}_{\text{diag}} \quad (15)$$

is a block-diagonal matrix containing the T-matrices of all particles,

$$\mathbf{T}_{\text{diag}} = \begin{pmatrix} \mathbf{T}_1 & \mathbb{O} & \cdots & \mathbb{O} \\ \mathbb{O} & \mathbf{T}_2 & \ddots & \vdots \\ \vdots & \ddots & \ddots & \mathbb{O} \\ \mathbb{O} & \cdots & \mathbb{O} & \mathbf{T}_N \end{pmatrix}, \text{ and } \mathbf{C}^{(3)} = \begin{pmatrix} \mathbb{O} & \mathbf{C}_{1,2}^{(3)} & \cdots & \mathbf{C}_{1,N}^{(3)} \\ \mathbf{C}_{2,1}^{(3)} & \mathbb{O} & \ddots & \vdots \\ \vdots & \ddots & \ddots & \mathbf{C}_{N-1,N}^{(3)} \\ \mathbf{C}^{(3)} & \cdots & \mathbf{C}_{N,N-1}^{(3)} & \mathbb{O} \end{pmatrix}. \quad (16)$$

Since matrix $\mathbf{T}_{\text{local}}$ accounts for interactions between multiple scatterers, it can already be used to simulate certain properties, such as CL and EEL probability per scatterer, as we demonstrate in the following section. To account for the total response from the entire cluster, one needs to convert the local T-matrix to a global matrix \mathbf{T} , where all fields are expanded around a single origin at $\mathbf{r}_0 = 0$. The global and incident field \mathbf{a} and scattered field \mathbf{p} coefficients are connected to the respective local ones via

$$\mathbf{a}_{\text{local}} = \left(\mathbf{C}_{1,0}^{(1)} \cdots \mathbf{C}_{N,0}^{(1)} \right) \mathbf{a} \quad (17a)$$

$$\mathbf{p} = \left(\mathbf{C}_{0,1}^{(1)} \cdots \mathbf{C}_{0,N}^{(1)} \right) \mathbf{p}_{\text{local}}, \quad (17b)$$

and the global matrix is given by

$$\mathbf{T} = \left(\mathbf{C}_{0,1}^{(1)} \cdots \mathbf{C}_{0,N}^{(1)} \right) \mathbf{T}_{\text{local}} \left(\mathbf{C}_{1,0}^{(1)} \cdots \mathbf{C}_{N,0}^{(1)} \right). \quad (18)$$

In Fig. 1(b), we mark the validity domain of the global description in a SWB with the red dotted circle, which lies outside the circumscribing sphere enclosing all scatterers [48]. Within this description, the impact parameter of the electron beam must be larger than the radius of this circumscribing sphere. However, this constraint does not apply when operating in the local basis.

Finally, we address structures with periodic boundaries in one dimension, such as the one depicted in Fig. 1(c). We demonstrated in Section II A that the field of the electron has a fixed wavevector component $k_z = k/\beta$ along its trajectory. Assuming a lattice L composed of a unit cell with N particles periodically arranged in space with pitch $\Lambda = \Lambda \hat{z}$ along the axis of the electron trajectory, the phase difference between unit cells is $e^{ik_z \Lambda}$. Then the scattered field amplitudes assume the form similar to Eq. (13), but now including a sum spanning over all lattice sites, as

$$\tilde{\mathbf{p}}_i = \mathbf{T}_i \left[\tilde{\mathbf{a}}_i + \underbrace{\sum_{j=1}^N \sum'_{\Lambda \in L} \mathbf{C}^{(3)}(\mathbf{r}_i - \mathbf{r}_j - \Lambda) e^{ik_z \Lambda} \tilde{\mathbf{p}}_j}_{\tilde{\mathbf{C}}_{i,j}^{(3)}} \right], \quad (19)$$

where the primed sum denotes the omission of the self-interaction term with $\Lambda = 0$ for $i = j$. In the local basis, and combining all scattered field expansions $\tilde{\mathbf{p}}_{\text{local}}$ analogously to Eq. (14), we have $\tilde{\mathbf{p}}_{\text{local}} = \mathbf{T}_{\text{local}} \tilde{\mathbf{a}}_{\text{local}}$, with $\mathbf{T}_{\text{local}} = [\mathbb{I} - \mathbf{T}_{\text{diag}} \tilde{\mathbf{C}}^{(3)}]^{-1} \mathbf{T}_{\text{diag}}$. Here, the matrix $\tilde{\mathbf{C}}^{(3)}$ is analogous to Eq. (16), but now with the diagonal blocks generally being non-zero and containing the interaction of the particle with its periodic equivalents. Figure 1(c) shows the validity domain of a local and a global description. The local spherical-wave expansions of the fields are valid outside the circumscribing sphere of each scatterer. The red dotted circles mark the domain of validity for a global T-matrix, describing the scatterers of a unit cell as a combined object. In a periodic arrangement, this description might be invalid due to overlapping circumscribing spheres, in which case only the local description can be employed.

C. Cathodoluminescence

During the interaction of an electron beam with a scatterer, a fraction of the kinetic energy of the electron that is transferred to the optical modes of the structure is radiated back to the environment. This emission is collected in CL spectroscopy, and is simulated by the respective probability $\Gamma_{\text{CL}}(\omega)$ of collecting a photon of energy $\hbar\omega$ in the far field. The CL probability can be calculated via the power of the electromagnetic fields radiating to the far field, integrated over a surface that encloses the structure. In the SWB, the enclosing surface is that of an arbitrarily large sphere with infinitesimal solid angle $d\Omega = \sin\theta d\theta d\phi$, and the CL probability is given by [50]

$$\Gamma_{\text{CL}}^{\text{S}}(\omega) = \frac{r^2}{\pi\hbar\omega} \oint d\Omega \operatorname{Re} \{ \mathbf{E}_{\text{sca}}(\mathbf{r}, \omega) \times \mathbf{H}_{\text{sca}}^*(\mathbf{r}, \omega) \} \cdot \hat{\mathbf{r}}. \quad (20)$$

By introducing the electric field expansion given in Eq. (7b), along with $\mathbf{H}_{\text{sca}}(\mathbf{r}, \omega) = \nabla \times \mathbf{E}_{\text{sca}}(\mathbf{r}, \omega) / (i\omega\mu_0)$, and in the limit $kr \rightarrow \infty$, we find

$$\Gamma_{\text{CL}}^{\text{S}}(\omega) = \frac{1}{\pi\hbar\omega Z} \frac{\mathbf{p}^\dagger \mathbf{p}}{k^2}, \quad (21)$$

where $Z = \sqrt{\mu_0/\epsilon_0}$ is the impedance in air.

In the CWB, the enclosing surface is that of a cylinder of length L and an infinitesimal normal surface element $\rho d\phi dz \hat{\mathbf{p}}$, yielding

$$\Gamma_{\text{CL}}^{\text{C}}(\omega) = \frac{\rho}{\pi\hbar\omega} \int_0^{2\pi} \int_0^L d\phi dz \operatorname{Re} \{ \mathbf{E}_{\text{sca}}(\mathbf{r}, \omega) \times \mathbf{H}_{\text{sca}}^*(\mathbf{r}, \omega) \} \cdot \hat{\mathbf{p}}. \quad (22)$$

Once again, we introduce Eq. (7b) and evaluate the field at $k_\rho \rho \rightarrow \infty$, to obtain

$$\Gamma_{\text{CL}}^{\text{C}}(\omega) = \frac{4L}{\pi\hbar\omega Z} \frac{\mathbf{p}^\dagger \mathbf{p}}{k}. \quad (23)$$

For structures that extend infinitely along the axis of the cylindrical waves, we can express the CL probability per unit length, namely Eq. (23) divided by the length L .

D. Electron energy loss

The measured quantity in EELS is the total electron energy loss, and is simulated by the respective probability of the electron losing energy $\hbar\omega$ while traveling against the scattered electromagnetic field, defined as

$$\Gamma_{\text{EEL}}(\omega) = \frac{e}{\pi\hbar\omega} \int_{-\infty}^{\infty} dt \operatorname{Re} \{ e^{-i\omega t} \mathbf{v} \cdot \mathbf{E}_{\text{sca}}(\mathbf{r}_e, \omega) \}. \quad (24)$$

By substituting in Eq. (24) the electric field expansion of Eq. (7b) in terms of spherical waves, we find

$$\Gamma_{\text{EEL}}^{\text{S}}(\omega) = -\frac{1}{\pi\hbar\omega Z} \frac{\text{Re}\{\mathbf{a}^\dagger \mathbf{p}\}}{k_0^2}, \quad (25)$$

whereas, by inserting the cylindrical wave expansion, we obtain

$$\Gamma_{\text{EEL}}^{\text{C}}(\omega) = \frac{4L}{\pi\hbar\omega Z} \frac{\text{Re}\{\mathbf{a}^T \mathbf{p}\}}{k_0}. \quad (26)$$

Similarly to the CL probability, for structures that extend infinitely along the axis of the cylindrical waves, we typically work with the EEL probability per unit length of electron trajectory, *i.e.*, Eq. (26) divided by the length L .

III. NUMERICAL IMPLEMENTATION AND EXAMPLES

In this section, we demonstrate the T-matrix formalism for CL and EELS simulations, as described in the previous sections, using a selected set of problems. To do so, we present here our extension of the in-house developed Python toolbox *treams*, designed for electromagnetic scattering computations using the T-matrix method. The open-source code is available at <https://github.com/tfp-photonics/treams> and a detailed description can be found in Ref. 48. This new module named *treams_ebeam* includes all functionalities of the original software, while adding electron beams as sources of illumination, and functions computing the relevant observable quantities. The open-source code for *treams_ebeam* is available at https://github.com/tfp-photonics/treams_ebeam. We also provide guidelines for using the module.

Within *treams_ebeam*, the electron beam source can be initialized with the wavenumber, reduced velocity, and impact parameter, as

```
>>> inc = treams_ebeam.ebeam(k0, vel, b)
```

which creates the singular cylindrical wave of Eq. (6). To expand the electron field as a regular field in the global CWB, we can use the `expand` operator:

```
>>> kz = k0/vel
>>> cwb = treams.CylindricalWaveBasis.default(kz, mmax)
>>> inc = inc.expand(cwb, 'regular')
```

To expand the field in the SWB, one has to first apply the above change of basis to expand around the origin of the global basis, and then convert to the SWB, using once again the `expand` operator:

```
>>> swb = treams.SphericalWaveBasis.default(lmax)
>>> inc = inc.expand(swb)
```

Given a T-matrix, the CL and EEL probability is calculated using the expressions that correspond to each basis as

```
>>> cl = treams_ebeam.cl(tmatrix, inc)
>>> eels = treams_ebeam.eels(tmatrix, inc)
```

For the `expand` operation to be performed correctly, the incident field and the T-matrix must be expressed in the same basis. The results of the `cl` and `eels` functions depend on the basis of the T-matrix; in the CWB, they correspond to CL and EEL probability per energy in eV and per unit length in nm, while in the SWB, per energy in eV. With the basic functionality established, we proceed to the examples.

A. Interaction with single scatterer

As our first example, we examine the CL and EEL spectra of single scatterers of different shapes and materials. Figure 2 shows the spectra for a non-dispersive dielectric sphere, an infinitely extended metallic cylinder (wire), and an elliptical nanodisk composed of amorphous silicon, considering an electron beam of reduced velocity $\beta = 0.7$, passing at a distance $R - b = 10$ nm from their surface.

Figure 2(a) shows the spectra of a dielectric sphere of radius $R = 50$ nm made from a material characterized by the nondispersive dielectric function $\epsilon = 16 + 0.5i$. In the energy window displayed, three optical modes can be observed, corresponding to the magnetic dipole, electric dipole, and magnetic quadrupole in increasing energy order. The difference between the EEL and CL curve reveals that a part of the energy is absorbed, rather than radiated, which is reasonable given the complex dielectric function. For this example, the T-matrix describing the sphere can be computed within *treams*, using the method `TMatrix.sphere`, as

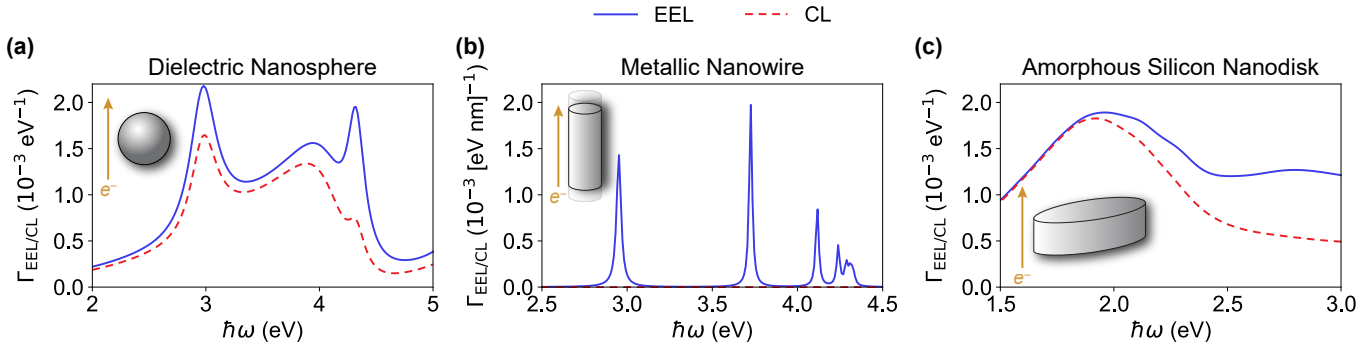


FIG. 2. EEL (blue solid line) and CL probability (red dashed line) of (a) a dielectric nanosphere of radius $R = 50$ nm, (b) a metallic nanowire of radius $R = 50$ nm and infinite length, and (c) an amorphous silicon elliptical nanodisk of height $h = 90$ nm, long axis $r_l = 286$ nm and short axis $r_s = 96$ nm. In all panels, we consider $R - b = 10$ nm and $\beta = 0.7$.

```
>>> tm = treams.TMatrix.sphere(lmax, k0, radius, materials)
```

Besides spheres, the T-matrices of infinite cylinders can be computed with the method `TMatrixC.cylinder`:

```
>>> kz = k0/vel
>>> tm = treams.TMatrixC.cylinder(kz, mmax, k0, radius, materials)
```

Figure 2(b) shows the spectra of a metallic wire of radius $R = 50$ nm whose dielectric function is given by the Drude model $\varepsilon(\omega) = \varepsilon_\infty - \omega_p^2/(\omega^2 + i\gamma_p\omega)$, with $\varepsilon_\infty = 3.3$, $\hbar\omega_p = 9$ eV and $\hbar\gamma_p = 22$ meV. The electron beam launches surface plasmon polaritons (SPPs), which are confined at the metal-air interface and propagate along it with wavenumber $k_z = k_0/\beta$. These take the form of purely TM cylindrical waves of different orders ($m = 0, 1, \dots, m_{\max}$), and appear in the spectra as Lorentzian peaks at different energies.

For geometries other than spheres and wires, the T-matrix can be calculated using alternative numerical methods. Most of the methods mentioned in Section I support this functionality. Once obtained, the T-matrix can be loaded into *treams*, provided that it complies with the specified format reported in Ref. 37. In Fig. 2(c), we show the response of an amorphous silicon elliptical nanodisk of height $h = 90$ nm, long axis $r_l = 286$ nm, and short axis $r_s = 96$ nm. This structure is inspired by Ref. 23, where such disks are arranged in a 2D lattice to investigate the emergence of BICs and q-BICs. In this example, the T-matrix is computed using the BEM-based MATLAB toolbox NANOSEM, with the dielectric function taken from Ref. 23, and can be found in the Daphona database [38]. The EEL and CL spectra in Fig. 2(c) show broad features rather than sharp Lorentzian peaks, and multipolar modes of mixed electric and magnetic type.

Given the T-matrix of individual scatterers, *treams* includes built-in methods to compute the T-matrix of periodic and aperiodic clusters, following the formulation described in Section II B. From the T-matrix of a simple or complex unit cell, the T-matrices of periodic nanoparticle arrays in one, two, and three dimensions are readily constructed by employing the highly efficient and fast converging Ewald method [48]. We next demonstrate simulations of CL and EELS in these scenarios.

B. Interaction with periodic chain of nanodisks

In this section, we demonstrate CL and EELS simulations of a finite and an infinite periodic chain of nanoparticles aligned in parallel to the electron trajectory. Periodic nanostructures are key building blocks for nanophotonic devices, because they support lattice interactions and resonances with enhanced quality factors, including plasmonic surface lattice resonances, BICs, and q-BICs. In the context of free electron–matter interactions, such configurations are widely studied as sources of Smith–Purcell radiation [44].

As a representative example, we arrange the amorphous silicon elliptical nanodisks introduced in Fig. 2(c) in a chain with pitch $\Lambda = 294$ nm along the z-axis, *i.e.*, parallel to the electron beam, as illustrated in Fig. 3. Figures 3(b) and 3(c) show the EEL and CL probability per nanoparticle, respectively, for finite chains containing $N = 1, 3, 5, 9$, and 15 nanoparticles, as well as for an infinite chain ($N = \infty$).

Starting from the T-matrix `disk` of a single object, the local T-matrix of Eqs. (15)–(16) of the finite chain, namely the cluster, containing multiple-scattering interactions among all objects, is computed in *treams* as:

```
>>> tm = treams.TMatrix.cluster([disk]*N, positions).interaction.solve()
```

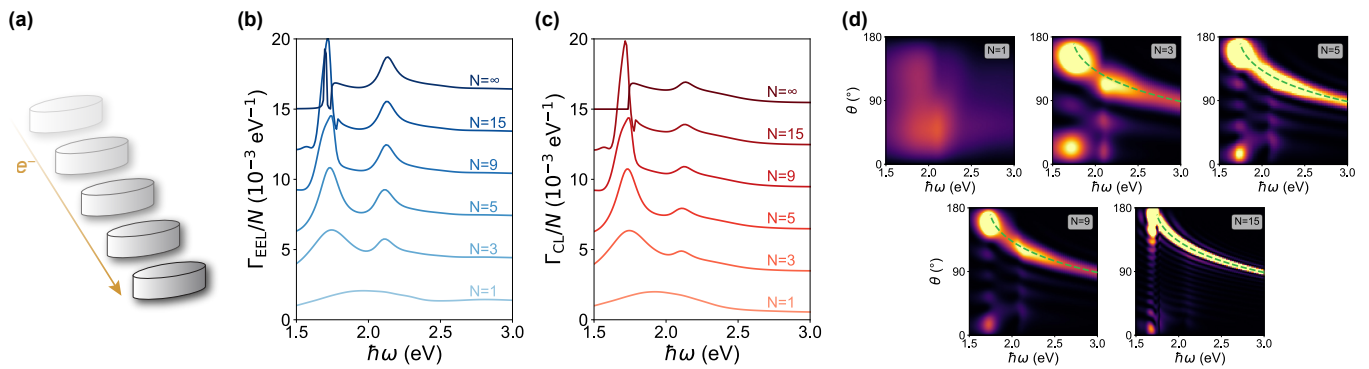


FIG. 3. (a) Schematic of the system under study: a chain of the amorphous silicon elliptical nanodisks excited by an electron beam with parameters $\beta = 0.7$ and $b - R = 7 \text{ nm}$. (b) EEL and (c) CL probabilities per nanoparticle for chains with $N = 1, 3, 5, 9, 15, \infty$ nanoparticles. Consecutive curves are vertically offset by $3 \cdot 10^{-3} \text{ eV}^{-1}$ for readability. (d) CL probability per nanoparticle versus azimuthal angle θ for the different cases of the finite chain. The dashed green lines trace the angles at which Smith-Purcell radiation is emitted in the first diffraction order.

To compute the CL and EEL probabilities, the incident electron field must first be expressed in the CWB at the positions of the nanoparticles and subsequently expanded into the SWB of the T-matrix. The outputs of `treams_ebeam.cl(tm, inc)` and `treams_ebeam.eels(tm, inc)` then yield the respective probabilities per unit cell, here per nanoparticle. Although it is possible to expand the T-matrix of the cluster from the local to the global basis, this operation will limit the validity of the computation to the domain outside the circumscribing sphere enclosing all scatterers, which is not compatible with the chosen impact parameter. Consequently, the EEL and CL calculations are performed within the local T-matrix `tm`.

For the infinite chain, the local T-matrix for a given lattice pitch and longitudinal component of the wavevector $k_z = k_0/\beta$ (where $\hbar k_z$ is the momentum transferred from the electron beam to the chain) is obtained by solving the interaction between periodic unit cells:

```
>>> lattice = treams.Lattice(pitch)
>>> chain = disk.latticeinteraction.solve(lattice, kz)
```

The resulting T-matrix `chain` is expressed in the SWB and can be used directly to calculate EEL probability per unit cell, using the `eels` method as described so far. Alternatively, the chain of periodic spherical waves transforms to a scattered cylindrical wave, thereby converting the T-matrix from a local SWB to a CWB with a single origin:

```
>>> cwb = treams.CylindricalWaveBasis.diffraction_orders(kz, lmax, lattice, bmax)
>>> chain_tmc = treams.TMatrixC.from_array(chain, cwb)
```

Here, the parameter $b_{\text{max}} = 2\pi n/\Lambda$ determines the diffraction orders n included in the simulation. In the CWB, Eqs. (23) and (26) yield the probabilities per unit length, while the corresponding probabilities per unit cell are obtained by multiplying by the lattice pitch.

As shown in Figs. 3(b) and 3(c), a lattice resonance emerges at approximately 1.7 eV due to the collective interactions among the nanodisks, becoming progressively sharper with each additional nanoparticle. In the infinite-chain limit (darkest blue and red curves), the radiative emission of this resonance is fully suppressed, as evidenced by the difference between CL and EEL spectra. In this regime, the CL emission arises from Smith-Purcell radiation, and photons of each energy are emitted in a cone of angle $\theta_n = \cos^{-1}(1/\beta - b_{\text{max}}(n)/k)$ for each diffraction order n ; here we set $n = 1$. Figure 2(d) shows the angular dependence of the CL emission for the different cases of the finite chain. While the emission from a single nanodisk is essentially omnidirectional, increasing the number of scatterers in the finite chain leads to progressively higher directionality, approaching the characteristic angular emission pattern of Smith-Purcell radiation, indicated with dashed green lines in the panels for $N = 3, 5, 9$, and 15. The nodes observed in the angular spectra correspond to the number of unit cells in the chain.

C. Interaction with finite 2D periodic array of nanospheres

As a final example, we explore the system shown in Fig. 4(a): an electron beam passing transversely through the center of a cluster of aluminum nanospheres arranged in a finite 2D array. All nanoparticles have radius $R = 50 \text{ nm}$, and permittivity given by the Drude model with $\varepsilon_{\infty} = 1$, $\hbar\omega_p = 15 \text{ eV}$ and $\hbar\gamma_p = 1.06 \text{ eV}$, while the square lattice

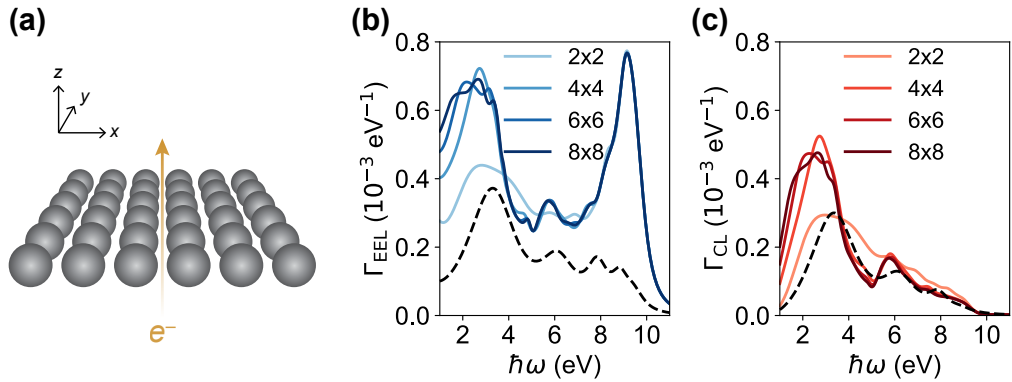


FIG. 4. (a) Schematic of the system under study: a finite 2D array of aluminum nanospheres is excited by an electron beam that passes transversely through its center with reduced velocity $\beta = 0.7$. (b) EEL and (c) CL probabilities for arrays consisting of $N = 2, 4, 6, 8$ nanoparticles per side. The black, dashed curves show the respective spectra for a single aluminum nanosphere positioned at the same distance from the electron trajectory as the nearest nanoparticle in the corresponding array.

pitch has a length of $\Lambda = 120$ nm. The T-matrix of each cluster is computed following the similar steps as for the finite chains presented in Section III B, for maximum multipole order $\ell_{\max} = 6$.

Lattice interactions in this case can be formed along multiple directions. In Figs. 4(b) and 4(c), we present the EEL (blue curves) and CL spectra (red curves), respectively, for different numbers of nanoparticles per side, compared to those of a single nanoparticle, positioned at the same distance from the electron trajectory as the nearest nanoparticle in the corresponding array (black dashed curves). In the EEL spectra of Fig. 4(b) for the single nanoparticle, we observe four Lorentzian peaks, three corresponding to $\ell = 1, 2, 3$, and one formed by overlapping modes with $\ell = 4-6$. Once arranged in the cluster, these features split into multiple peaks, due to bonding and antibonding hybridization of plasmonic modes among the nanoparticles. In the curve corresponding to an array with two nanoparticles ($N = 2$) per side, this splitting of the electric dipole mode is not resolved because the peaks lie very close in energy, appearing as a single broad resonance at 2.8 eV. Then, at 9.1 eV we observe a high-intensity peak, emerging from the interaction between the overlapping higher-order modes. Naturally, this feature is not present in the CL spectra of Fig. 4(c), as higher-order modes are very tightly confined on the surface of the individual nanoparticles, and generally do not radiate.

Adding an extra two nanoparticles ($N = 4$) per side results in a more intense resonance at lower energies, since now more nanoparticles are excited. Further increasing the number of nanoparticles does not yield substantial qualitative changes in the spectra, other than a better resolution of the individual peaks at low energies. This is because the field produced by the electron is evanescent in the plane of the array and therefore couples weakly to nanoparticles farther from its trajectory. This coupling is even weaker for higher-order modes. Eventually, only a limited number of nanoparticles is excited and thus participate in the formation of the lattice resonance. At the same time, in the EEL spectra of Fig. 4(b), the contribution of higher-order modes remains essentially unchanged for all sizes of arrays.

IV. CONCLUSIONS

We presented a T-matrix-based scattering formulation for modeling the interaction of fast electrons with single or multiple scatterers. Starting from the expansion of the field generated by a fast electron in the CWB, we related this source to the response of a nanostructure via the T-matrix formalism, and provided generalized formulas addressing finite and infinite 1D periodic arrays. Using these formulas, we derived expressions for computing the CL and EEL probabilities. We implemented the electron-beam spectroscopy functionality in the existing *treams* open-source software suite for electromagnetic scattering computations as an add-on module called *treams_ebeam*. To demonstrate both the method and the software, we explored three representative examples: single scatterers, finite arrays, and infinite periodic arrays of scatterers, providing guidelines for using the module. We envision this tool serving as a user-friendly resource for CL and EELS simulations.

V. ACKNOWLEDGEMENTS

We thank N. Asadova, J. D. Fischbach, K. Frizyuk, M. Gabbert, P. Garg, E. Herzog, L. Rebholz, and N. Ustimenko, for providing technical assistance and valuable feedback on the results. P. E. S. is supported by a research grant (VIL71383) from VILLUM FONDEN.

* elli.stamatopoulou@kit.edu

† carsten.rockstuhl@kit.edu

[1] F. J. García de Abajo, Optical excitations in electron microscopy, *Rev. Mod. Phys.* **82**, 209 (2010).

[2] M. Kociak and L. F. Zagonel, Cathodoluminescence in the scanning transmission electron microscope, *Ultramicroscopy* **176**, 112 (2017).

[3] T. Coenen and N. M. Haegel, Cathodoluminescence for the 21st century: Learning more from light, *App. Phys. Rev.* **4**, 031103 (2017).

[4] R. F. Egerton, *Electron Energy-Loss Spectroscopy in the Electron Microscope*, 3rd ed. (Springer Science+Business Media, New York, 2011).

[5] A. Polman, M. Kociak, and F. J. García de Abajo, Electron-beam spectroscopy for nanophotonics, *Nat. Mater.* **18**, 1158 (2019).

[6] F. J. García de Abajo and V. Di Giulio, Optical excitations with electron beams: Challenges and opportunities, *ACS Photonics* **8**, 945 (2021).

[7] H. Watanabe, Experimental evidence for the collective nature of the characteristic energy loss of electrons in solids –Studies on the dispersion relation of plasma frequency–, *J. Phys. Soc. Japan* **11**, 112 (1956).

[8] R. H. Ritchie, Plasma losses by fast electrons in thin films, *Phys. Rev.* **106**, 874 (1957).

[9] N. Yamamoto, K. Araya, and F. J. García de Abajo, Photon emission from silver particles induced by a high-energy electron beam, *Phys. Rev. B* **64**, 205419 (2001).

[10] E. J. R. Vesseur, R. de Waele, M. Kuttge, and A. Polman, Direct observation of plasmonic modes in Au nanowires using high-resolution cathodoluminescence spectroscopy, *Nano Lett.* **7**, 2843 (2007).

[11] T. Coenen, J. van de Groep, and A. Polman, Resonant modes of single silicon nanocavities excited by electron irradiation, *ACS Nano* **7**, 1689 (2013).

[12] T. Matsukata, N. Matthaiakakis, T.-a. Yano, M. Hada, T. Tanaka, N. Yamamoto, and T. Sannomiya, Selection and visualization of degenerate magnetic and electric multipoles up to radial higher orders by cathodoluminescence, *ACS Photonics* **6**, 2320 (2019).

[13] S. Fiedler, P. E. Stamatopoulou, A. Assadillayev, C. Wolff, H. Sugimoto, M. Fujii, N. A. Mortensen, S. Raza, and C. Tserkezis, Disentangling cathodoluminescence spectra in nanophotonics: Particle eigenmodes vs transition radiation, *Nano Lett.* **22**, 2320 (2022).

[14] M. J. Lagos, A. Trigler, U. Hohenester, and P. E. Batson, Mapping vibrational surface and bulk modes in a single nanocube, *Nature* **543**, 529 (2017).

[15] F. S. Hage, D. M. Kepaptsoglou, Q. M. Ramasse, and L. J. Allen, Phonon spectroscopy at atomic resolution, *Phys. Rev. Lett.* **122**, 016103 (2019).

[16] A. A. Govyadinov, A. Konečná, A. Chuvilin, S. Vélez, I. Dolado, A. Y. Nikitin, S. Lopatin, F. Casanova, L. E. Hueso, J. Aizpurua, *et al.*, Probing low-energy hyperbolic polaritons in van der waals crystals with an electron microscope, *Nat. Commun.* **8**, 95 (2017).

[17] C. Maciel-Escudero, A. Konečná, R. Hillenbrand, and J. Aizpurua, Probing and steering bulk and surface phonon polaritons in uniaxial materials using fast electrons: Hexagonal boron nitride, *Phys. Rev. B* **102**, 115431 (2020).

[18] D. Kepaptsoglou, J. Á. Castellanos-Reyes, A. Kerrigan, J. Alves do Nascimento, P. M. Zeiger, K. El Hajraoui, J. C. Idrobo, B. G. Mendis, A. Bergman, V. K. Lazarov, *et al.*, Magnon spectroscopy in the electron microscope, *Nature* **644**, 83 (2025).

[19] S. J. Smith and E. M. Purcell, Visible light from localized surface charges moving across a grating, *Phys. Rev.* **92**, 1069 (1953).

[20] J. B. Pendry and L. Martin-Moreno, Energy loss by charged particles in complex media, *Phys. Rev. B* **50**, 5062 (1994).

[21] F. Chen, R.-H. Fan, J.-X. Chen, Y. Liu, B.-Q. Hou, R.-W. Peng, and M. Wang, Tuning smith–purcell radiation by rotating a metallic nanodisk array, *Opt. Lett.* **48**, 2002 (2023).

[22] F. J. García de Abajo, A. G. Pattantyus-Abraham, N. Zabala, A. Rivacoba, M. O. Wolf, and P. M. Echenique, Cherenkov effect as a probe of photonic nanostructures, *Phys. Rev. Lett.* **91**, 143902 (2003).

[23] Z. Dong, Z. Mahfoud, R. Paniagua-Domínguez, H. Wang, A. I. Fernández-Domínguez, S. Gorelik, S. T. Ha, F. Tjiptoharsono, A. I. Kuznetsov, M. Bosman, and J. K. W. Yang, Nanoscale mapping of optically inaccessible bound-states-in-the-continuum, *Light Sci. Appl.* **11**, 20 (2022).

[24] F. J. García de Abajo and A. Howie, Retarded field calculation of electron energy loss in inhomogeneous dielectrics, *Phys. Rev. B* **65**, 115418 (2002).

[25] U. Hohenester, Simulating electron energy loss spectroscopy with the MNPBEM toolbox, *Comput. Phys. Commun.* **185**, 1177 (2014).

[26] C. Maciel-Escudero, A. B. Yankovich, B. Munkhbat, D. G. Baranov, R. Hillenbrand, E. Olsson, J. Aizpurua, and T. O. Shegai, Probing optical anapoles with fast electron beams, *Nat. Commun.* **14**, 8478 (2023).

[27] P. Das, T. K. Chini, and J. Pond, Probing higher order surface plasmon modes on individual truncated tetrahedral gold nanoparticle using cathodoluminescence imaging and spectroscopy combined with FDTD simulations, *J. Phys. Chem. C* **116**, 15610 (2012).

[28] Y. Cao, A. Manjavacas, N. Large, and P. Nordlander, Electron energy-loss spectroscopy calculation in finite-difference time-domain package, *ACS Photonics* **2**, 369 (2015).

[29] A. A. Kichigin and M. A. Yurkin, Simulating electron energy-loss spectroscopy and cathodoluminescence for particles in arbitrary host medium using the discrete dipole approximation, *J. Phys. Chem. C* **127**, 4154 (2023).

[30] C. Matyssek, J. Niegemann, W. Hergert, and K. Busch, Computing electron energy loss spectra with the discontinuous Galerkin time-domain method, *Photon. Nanostruct. Fundam. Appl.* **9**, 367 (2011).

[31] M. Husnik, F. von Cube, S. Irsen, S. Linden, J. Niegemann, K. Busch, and M. Wegener, Comparison of electron energy-loss and quantitative optical spectroscopy on individual optical gold antennas, *Nanophotonics* **2**, 241 (2013).

[32] M. Prämassing, T. Kiel, S. Irsen, K. Busch, and S. Linden, Electron energy loss spectroscopy on freestanding perforated gold films, *Phys. Rev. B* **103**, 115403 (2021).

[33] P. E. Stamatopoulou, W. Zhao, A. Rodríguez Echarri, N. A. Mortensen, K. Busch, C. Tserkezis, and C. Wolff, Electron beams traversing spherical nanoparticles: Analytic and numerical treatment, *Phys. Rev. Res.* **6**, 013239 (2024).

[34] P. C. Waterman, Matrix formulation of electromagnetic scattering, *Proc. IEEE* **53**, 805 (1965).

[35] M. I. Mishchenko, L. D. Travis, and D. W. Mackowski, T-matrix method and its applications to electromagnetic scattering by particles: A current perspective, *J. Quant. Spectrosc. Radiat. Transf.* **111**, 1700–1703 (2010).

[36] M. I. Mishchenko, G. Videen, V. A. Babenko, N. G. Khlebtsov, and T. Wriedt, T-matrix theory of electromagnetic scattering by particles and its applications: a comprehensive reference database, *J. Quant. Spectrosc. Radiat. Transf.* **88**, 357–406 (2004).

[37] N. Asadova, K. Achouri, K. Arjas, B. Auguié, R. Aydin, A. Baron, D. Beutel, B. Bodermann, K. Boussaoud, S. Burger, *et al.*, T-matrix representation of optical scattering response: Suggestion for a data format, *J. Quant. Spectrosc. Radiat. Transf.* **333**, 109310 (2025).

[38] N. Asadova, K. Boussaoud, J. Meyer, F. Tristram, and C. Rockstuhl, A t-matrix database to promote information-driven research in nanophotonics, arXiv preprint arXiv:2602.02101 [10.48550/arXiv.2602.02101](https://arxiv.org/abs/2602.02101) (2026).

[39] D. W. Mackowski and M. I. Mishchenko, Calculation of the T matrix and the scattering matrix for ensembles of spheres, *J. Opt. Soc. Am. A* **13**, 2266 (1996).

[40] Y.-l. Xu, Electromagnetic scattering by an aggregate of spheres, *Appl. Opt.* **34**, 4573 (1995).

[41] I. Fernandez-Corbaton, An algebraic approach to light–matter interactions, *Adv. Phys. Res.* **4**, 2400088 (2025).

[42] R. Alaee, C. Rockstuhl, and I. Fernandez-Corbaton, Exact multipolar decompositions with applications in nanophotonics, *Adv. Opt. Mater.* **7**, 1800783 (2019).

[43] F. J. García de Abajo, Relativistic energy loss and induced photon emission in the interaction of a dielectric sphere with an external electron beam, *Phys. Rev. B* **59**, 3095 (1999).

[44] F. J. García de Abajo, Smith-purcell radiation emission in aligned nanoparticles, *Phys. Rev. E* **61**, 5743 (2000).

[45] N. Zabala, A. Rivacoba, and P. M. Echenique, Energy loss of electrons travelling through cylindrical holes, *Surf. Sci.* **209**, 465 (1989).

[46] C. A. Walsh, An analytical expression for the energy loss of fast electrons travelling parallel to the axis of a cylindrical interface, *Philos. Mag. B* **63**, 1063 (1991).

[47] Á. Rodríguez Echarri, W. Zhao, K. Busch, and F. J. García de Abajo, Relativistic electron energy-loss spectroscopy in cylindrical waveguides and holes, *Phys. Rev. B* **111**, 205436 (2025).

[48] D. Beutel, I. Fernandez-Corbaton, and C. Rockstuhl, treams – A T-matrix-based scattering code for nanophotonics, *Comput. Phys. Commun.* **297**, 109076 (2024).

[49] C. F. Bohren and D. R. Huffman, *Absorption and Scattering of Light by Small Particles* (John Wiley & Sons, New York, 1983).

[50] P. E. Stamatopoulou, C. Maciel-Escudero, N. A. Mortensen, C. Rockstuhl, and C. Tserkezis, Analytic methods in electron energy-loss and cathodoluminescence spectroscopy of planar and spherical nanostructures: tutorial, *J. Opt. Soc. Am. B* **42**, 1620 (2025).

[51] H. Huang, L. Tsang, A. Colliander, and S. H. Yueh, Propagation of waves in randomly distributed cylinders using three-dimensional vector cylindrical wave expansions in foldy–lax equations, *IEEE J. Multiscale Multiphysics Comput. Tech.* **4**, 214 (2019).

[52] G. Han, Y. Han, and H. Zhang, Relations between cylindrical and spherical vector wavefunctions, *J. Opt. A: Pure Appl. Opt.* **10**, 015006 (2007).